14th International Symposium on Turbulence and Shear Flow Phenomena (TSFP14)
Heidelberg, Germany, July 28–31, 2026

SUPERSATURATION FLUCTUATIONS IN STRATOCUMULUS CLOUDS

Robert Hartmann & Juan Pedro Mellado

Department of Earth System Sciences – Meteorology
University of Hamburg
Bundestraße 55, 20146 Hamburg, Germany

robert.hartmann@uni-hamburg.de
juan.pedro.mellado@uni-hamburg.de

ABSTRACT

Most simulations of atmospheric flows assume phase equilibrium between the liquid and the vapor phases of water. This assumption implies infinitely fast relaxation processes for supersaturation fluctuations – a condition that is not anymore fulfilled on meter and sub-meter length scales of turbulent atmospheric flows. Here, we investigate how a ”slow” saturation adjustment alters the flow dynamics and drives the formation of supersaturation fluctuations in a stratocumulus topped convective boundary layer.

We conduct direct numerical simulations of a stratocumulus topped boundary layer at Reynolds number $\mathrm{Re} = 5000$ with a one-moment bulk formulation of evaporation-condensation. First, 2D cases are carried out to validate implicit time stepping variants for the evaporation term. Then, a 3D case with slow saturation adjustment is compared to the case with phase equilibrium assumption . The comparison reveals that supersaturation is limited to upward transport inside the cloud layer and peaks in the updrafts at the cloud base, where q_l is still small. Analyzing the joint PDFs of RH, q_l and w, we found that subsaturation is more important than supersaturation for the evolution of the cloud's water content. Based on our findings, we argue that with finite saturation adjustment clouds tend to accumulate more water than with phase equilibrium assumption.

INTRODUCTION

Convection in the atmospheric boundary layer is characterized by the presence of water in different phases. The release and absorption of latent heat due to evaporation and condensation affect the energy budget of the system and significantly influence its dynamics – most evidently in the formation of clouds. Most simulations of atmospheric phenomena – including both large-eddy simulations (LES) and direct numerical simulations (DNS) – assume an infinitely fast saturation adjustment to equilibrium between the liquid and the vapor phases of water. This, however, implies that the adjustment processes act on by far shorter time scales than turbulent mixing, which does not hold on sub-meter length scales of turbulent atmospheric flows (Siebesma *et al.*, 2020; Rogers & Yau, 1996). Here, we investigate the influence of a finite saturation adjustment on the flow dynamics and the occurrence of supersaturation fluctuations in stratocumulus clouds.

Stratocumulus clouds play an important two-fold role in the Earth's climate as they can have a cooling effect by reflecting large portions of solar radiation to space on the one hand, but keeping the surface heat at night on the other hand. These clouds are characterized by a strong capping inversion at the cloud top, which leads to dominant turbulence scales on the order of meters or less (Wood, 2012; Mellado, 2017). This also calls for an accurate representation of their formation and lifetime in climate projections, which likely will improve with a better understanding of the role of supersaturation fluctuations (Wood, 2012; Nuijens & Siebesma, 2019).

The relative importance of supersaturation fluctuations can be quantified in terms of a Damköhler number $\mathrm{Da} = \tau_{fl}/\tau_{ph}$ defined as the ratio of the flows mixing time scale τ_{fl} over the phase relaxation time scale of supersaturation τ_{ph} (Shaw, 2003). From a physical point of view, this Damköhler number is typically used to distinguish between two regimes (i) of ”fast microphysics” for $\mathrm{Da} \gg 1$, where supersaturation adjustment is much faster than mixing, and (ii) of ”slow microphysics” for $\mathrm{Da} \ll 1$, where mixing happens much faster than microphysical adjustment. From a fluid dynamical perspective, these two regimes with (likely) different flow characteristics, will potentially be connected via a third ”transitional” regime around $\mathrm{Da} \approx \mathscr{O}(1)$. While the assumption of phase equilibrium corresponds to $\mathrm{Da} \to \infty$, estimates for typical atmospheric conditions cover $\tau_{fl} = \mathscr{O}(10^{-1} - 10^{2}\ \mathrm{s})$ and $\tau_{ph} = \mathscr{O}(10^{-1} - 10^{1}\ \mathrm{s})$ (e.g., Chandrakar *et al.*, 2016; Mellado, 2017; Cooper, 1989), which yields $\mathrm{Da} = \mathscr{O}(10^{-2} - 10^{3})$. However, since turbulent mixing acts on a range of time scales from integral time scale $\tau_0 = l_0/U_0$ of large eddies to Kolmogorov time scale $\tau_\eta = \tau_0/\sqrt{\mathrm{Re}}$ of the smallest eddies, it remains difficult to qualitatively evaluate the importance of supersaturation fluctuations based on a single τ_{fl} or Da. This means that while large eddies still obey to ”fast” microphysics, the smallest eddies can already follow the dynamics of ”slow” microphysics.

High-resolution state-of-the-art DNSs of stratocumulus topped boundary layer (STBL) achieve Reynolds numbers Re up to $\mathscr{O}(10^4)$ (e.g., Pistor & Mellado, 2025) corresponding to Kolmogorov time scales $\tau_\eta = \mathscr{O}(10^0 - 10^1\,\mathrm{s})$, which yields $\mathrm{Da}_\eta = \mathscr{O}(10^{-1} - 10^{1})$ on the smallest flow scales, indicating that supersaturation fluctuations start to become important. In this study, we analyze the impact of ”slow” saturation adjustment on the cloud dynamics and flow characteristics in DNSs of a STBL with $\mathrm{Re} = 5 \cdot 10^3$ for $\mathrm{Da}_\eta \approx 0.14$ compared to the case with phase equilibrium assumption.

BULK FORMULATION OF EVAPORATION AND CONDENSATION

The governing set of equations describing a STBL under anelastic approximation comprise the continuity equation, Navier-Stokes equations, and evolution equations for liquid-water static energy h, total specific humidity q_t, and liquid specific humidity q_l, which determine the buoyancy field (e.g., Mellado *et al.*, 2018). The supersaturation fluctuations are represented by the evaporation-condensation term in the evolution equation of q_l, which, in general nondimensional anelastic form, can be modeled as:

$$\frac{l_0}{\rho_0 U_0}\left(\partial_t \rho q_l\right)_{con} = \frac{1}{\rho_z}\,\mathrm{Da}_0\,(\rho_z\, q_l)^{\gamma+1}\left(\frac{1}{q_s}\frac{q_t-q_l}{1-q_l}-1\right) \quad (1)$$

Therein, ρ_0, l_0, and U_0 are the reference density, height, and velocity, which are used for the normalization; ρ_z is the vertical background density profile; q_s denotes the saturation vapor specific humidity; and Da_0 and γ are the Damköhler number with respect to the integral model scales and modifying adjustment exponent, respectively, which both depend on the chosen framework for saturation adjustment. In the following, we introduce two different frameworks. First, considering droplets of a fixed diameter d_v, their phase relaxation time can be approximated as $\tau_{p,0} = d_v^2/(12\kappa_d)$, where $\kappa_d \approx 10^{-10}$ m^2/s depicts an effective droplet diffusivity (Rogers & Yau, 1996). In this case, it remains $\gamma = 0$ and the effective Damköhler number is defined as

$$\mathrm{Da}_0 \equiv \mathrm{Da}_{0,d_v} = \frac{l_0/U_0}{\tau_{p,0}}\,\frac{1}{\alpha_{\mathrm{DSD}}} = \frac{12\kappa_d l_0}{d_v^2 U_0}\,\frac{1}{\alpha_{\mathrm{DSD}}} \quad (2)$$

where the factor α_{DSD} accounts for the effect of droplets of varying diameter d. Second, considering a fixed number density of droplets n_d instead, their (volumetric mean) diameter d_v per grid cell is given by $d_v(n_d,\rho q_l) = \left(\frac{6\rho q_l}{\pi \rho_l n_d}\right)^{1/3}$. Substituting this in Eq. 2 yields

$$\mathrm{Da}_0 \equiv \mathrm{Da}_{0,n_d} = \frac{12\kappa_d l_0}{U_0}\left(\frac{6\rho_0}{\pi \rho_l n_d}\right)^{-2/3}\frac{1}{\alpha_{\mathrm{DSD}}} \quad (3)$$

together with $\gamma = -2/3$. In both cases, the factor $\alpha_{\mathrm{DSD}} = \overline{d^3}/(\overline{d}\,\overline{d_v^2})$ is determined via the third and first moments of the droplet size distribution (DSD). While for monodisperse droplets simply $\alpha_{\mathrm{DSD}}^{-1} = 1$, assuming a log-normal DSD results in $\alpha_{\mathrm{DSD}}^{-1} = \exp(-\sigma^2)$, where σ is the width of the DSD.

The definitions above describe the Damköhler number with respect to the integral reference scales of the system. Physically, however, an interaction between saturation adjustment and turbulence begins at the smallest flow scales. Applying $l_0/U_0 = \tau_0 = \sqrt{\mathrm{Re}}\;\tau_\eta$ relates the Damköhler number $\mathrm{Da}_0 = \mathrm{Re}^{1/2}\mathrm{Da}_\eta$ to the Kolmogorov scales in both cases.

NUMERICAL SETUP

The governing equations of a STBL in anelastic approximation are solved with our in-house code *ATLab* using 6th order compact finite-differences and a 4th order explicit Runge Kutta scheme. *ATLab* is openly available on *GitHub* (`https://github.com/turbulencia/atlab`). The code has been expanded by the above non-equilibrium formulation of evaporation and condensation (Eq. 1) to account

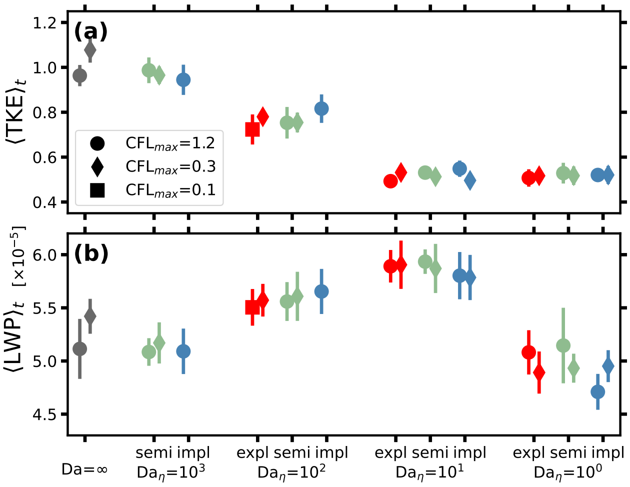

Figure 1. Time-averaged integral quantities of **(a)** dimensionless turbulent kinetic energy (TKE) and **(b)** dimensionless liquid water path (LWP) for the explicit, semi-implicit, and fully implicit evaporation schemes at various Da_{η,d_v} and time stepping (CFL) conditions. All cases are 2D with $\mathrm{Re} = 5000$. The averaging interval spans $10 \leq t/\tau_0 \leq 25$.

for supersaturation fluctuations. We note that due to $q_l = 0$ in significant parts of the domain, an effective exponent of $1/3 < 1$ requires an implicit time stepping of the evaporation term when using the n_d-framework.

Therefore, we utilize time splitting and consider the evaporation term differently from the remainder of the governing equations. In particular, an implicit Euler scheme for q_l is added at the end of each Runge-Kutta substage (which is used for the global time stepping):

$$q_l^{(n+1)} = q_l^{(n+1)_{\mathrm{expl}}} + \Delta t^{(n)} \cdot f_{con}\left(q_s^{(n+1)}, q_l^{(n+1)}, q_t^{(n+1)}\right) \quad (4)$$

In there, the superscripts indicate the time step of the various time-dependent quantities, such that $q_l^{(n+1)_{\mathrm{expl}}}$ is the solution of the explicit terms in the q_l-equation, $\Delta t^{(n)}$ the simulation time step, and $f_{con}(q_s^{(n+1)}, q_l^{(n+1)}, q_t^{(n+1)})$ the implicit contribution by the evaporation term. Solving is handled by an iterative Newton-Raphson scheme, which means that, nominally, we loose the 4th order accuracy.

In our simulations, we mostly particularize the conditions of *DYCOMS-II* flight RF01 (Stevens *et al.*, 2005, 2003) using, e.g., $l_0 = 840$ m for the reference inversion height of the STBL and $U_0 = 1.180$m/s (for further details on the particularization see Pistor & Mellado, 2025; Mellado *et al.*, 2018). Sedimentation effects are not considered here. The computational domains have a size of $L_x \times L_z = 8l_0 \times 2.5l_0$ and $L_x \times L_y \times L_z = 8l_0 \times 8l_0 \times 2.5l_0$ for the 2D and 3D cases, respectively, with periodic horizontal boundary conditions. At the bottom, a no-slip boundary condition is employed together with constant scalar fluxes. At the top, kinematic free-slip and constant flux boundary conditions are imposed. For the chosen $\mathrm{Re} = 5 \cdot 10^3$ (corresponding to a resolved Kolmogorov scale of $\eta \approx 1.4$ m), the computational grid consists of $N_x \times N_z = 3072 \times 768$, resp. $N_x \times N_y \times N_z = 3072 \times 3072 \times 768$ grid points applying a hyperbolic tangent like stretching of grid points in the vertical direction above $z/l_0 = 1$ and clustering towards the bottom.

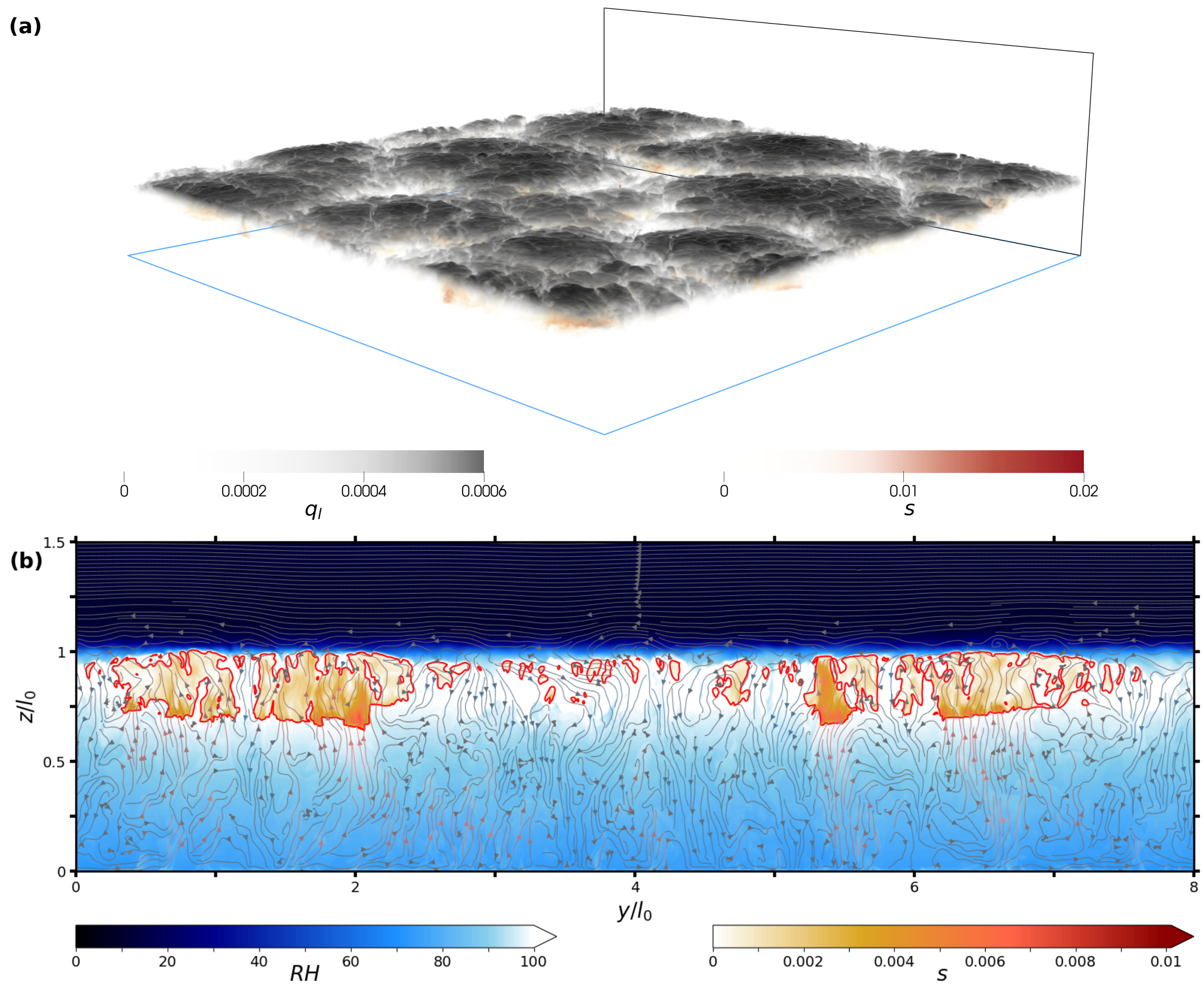

Figure 2. **(a)** 3D snapshot of liquid specific humidity q_l and supersaturation s for $\mathrm{Da}_{0,n_d} = 10$ with $\mathrm{Re} = 5000$ and **(b)** vertical slice marked in (a) showing relative humidity $RH = 100 \cdot \frac{q_t - q_l}{q_s}$, resp. supersaturation $s = \frac{q_t - q_l}{q_s} - 1$ overlayed with the streamlines of the instantaneous flow field. The red contour at $RH = 100 \Leftrightarrow s = 0$ encircle regions of supersaturation. The streamlines are color-coded by the amplitude of the vertical velocity component as a guide to the eye emphasizing ascending (reddish), horizontal (grayish), and descending flow (blueish). The upper part of the domain ($1.5 \leq z/l_0 \leq 2.5$) is not shown here, in order to focus on the dynamical structures around the inversion height $z/l_0 = 1$.

Validation of evaporation scheme

In a first step, we validate the implicit time stepping for evaporation by comparing the results to those from an explicit time stepping (Fig. 1). To do so, we need to retain $\gamma = 0$, i.e., in the fixed d_v-framework with $\mathrm{Da}_{0,d_v} = \mathrm{Re}^{1/2}\mathrm{Da}_{\eta,d_v}$. We test two variants of the implicit Euler scheme: (i) a fully implicit time stepping, where the saturation vapor humidity $q_s^{(n+1)} = f(T(h^{(n+1)}, q_t^{(n+1)}, q_l^{(n+1)}))$ is updated at the beginning of each Newton-Raphson iteration based on the updated q_l, and (ii) a semi-implicit time stepping, where $q_s^{(n+1)} = f(T^{\mathrm{expl}})$ is calculated only once per Runge-Kutta substage based on the explicit solutions $h^{(n+1)}$, $q_t^{(n+1)}$, and $f_{\mathrm{expl}}(q_l^{(n)})$.

The validation is performed using 2D cases. Fig. 1 shows the volume-integrated quantities of turbulent kinetic energy (TKE) and liquid water content (liquid water path, LWP) averaged over 15 τ_0 after an initial transient of 10 τ_0 for the three schemes at various Da_{η,d_v} and time stepping (CFL) conditions. Per Da_{η,d_v} the results of the different schemes vary just within their own statistical error independent of the maximum CFL condition, which proves the general accuracy of our implicit scheme(s) despite the reduced order of accuracy. In particular, we want to note that the results of the two implicit variants are basically indistinguishable. Hence and regarding the lower computational workload, we favor the semi-implicit variant. Fig. 1 further shows that towards larger Da an explicit time stepping of evaporation requires smaller time steps due to numerical stability, while the implicit time stepping variants allow to maintain the large time steps. Furthermore, towards large Da, TKE and LWP converge to the results obtained with the equilibrium approach (Fig. 1: gray data points, $\mathrm{Da} = \infty$).

Evaporation in DYCOMS-II

For the remainder of the paper, we focus on the role of evaporation-condensation in the DYCOMS-II case (Stevens *et al.*, 2005, 2003). In numerical studies of this reference case, it is customary to consider the number density n_d given, as it is better constrained (Ackerman *et al.*, 2004; Bretherton *et al.*, 2007; Schulz & Mellado, 2019). Hence, we switch to the fixed n_d-framework ($\gamma = -2/3$). For DYCOMS-II flight RF01, the number density concentration is estimated as $n_d =$

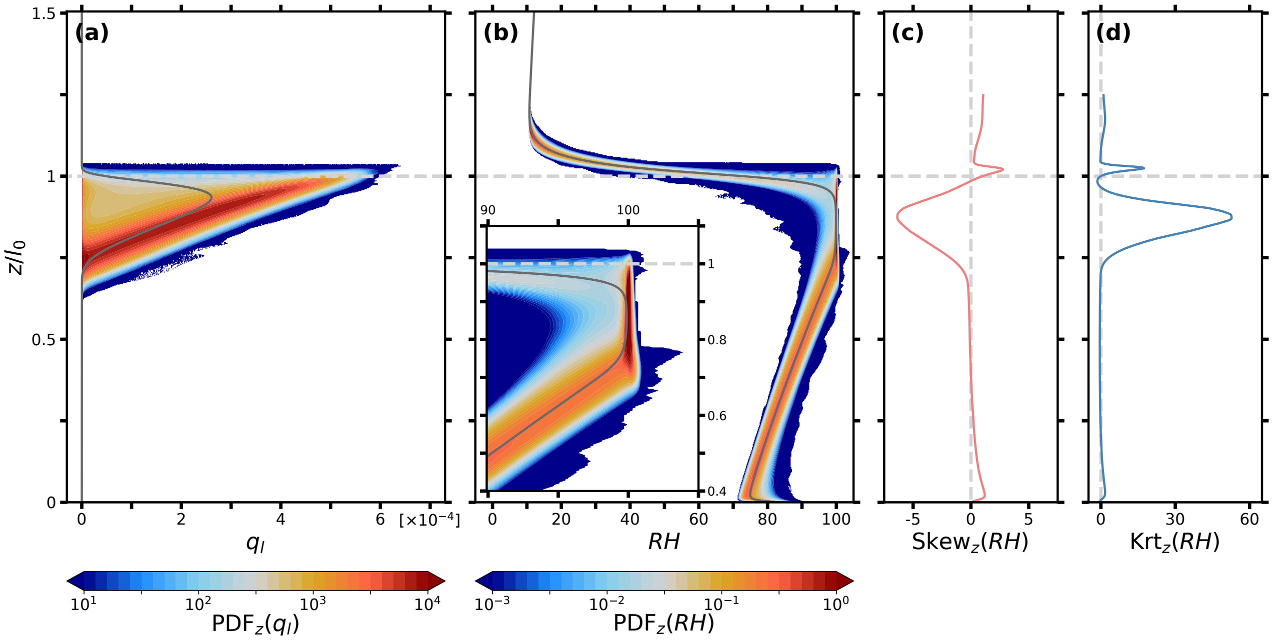

Figure 3. Probability density functions (PDFs) of **(a)** liquid specific humidity q_l and **(b)** relative humidity RH per height z/l_0 for $\mathrm{Da}_{0,n_d} = 10$ and $\mathrm{Re} = 5000$ from eight snapshots. The gray lines in (a) and (b) are the vertical profiles of the mean q_l and RH, respectively. **(c)** and **(d)** show the corresponding vertical profiles of relative humidity's skewness $\mathrm{Skew}_z(RH)$ and excess kurtosis $\mathrm{Krt}_z(RH)$ (i.e., $\mathrm{Krt} = 0 \,\widehat{=}\,$ Gaussian).

140 cm^{-3} while typical values ranges from $n_d = 100$ cm^{-3} for clean air to $n_d = 1000$ cm^{-3} for polluted air (Ackerman *et al.*, 2004; Bretherton *et al.*, 2007; Schulz & Mellado, 2019). For the DSD width typical values range from $\sigma = \ln(1)$ to $\sigma = \ln(1.5)$. Altogether, these ranges result into Damköhler numbers $9 \lesssim \mathrm{Da}_{0,n_d} \lesssim 50$. Therefore, we consider $\mathrm{Da}_{0,n_d} = 10$ ($\mathrm{Da}_{\eta,n_d} \approx 0.14$ for the chosen $\mathrm{Re} = 5000$), i.e., the lower limit of Damköhler estimates, and compare it to the results from an equilibrium ($\mathrm{Da} = \infty$) run. The following comparison is based on 3D simulations.

RESULTS

First, we will identify were supersaturation occurs. The $\mathrm{Da}_{0,n_d} = 10$ case shows that a realistic saturation adjustment, i.e., considering q_l as additional prognostic quantity with a finite evaporation-condensation term, can produce a widely supersaturated cloud layer with regions of relative humidity $RH > 100$ (Fig. 2). Supersaturation is limited to the cloud layer at $0.6 \lesssim z/l_0 \lesssim 1$ and therein mostly correlating with ascending flow (Fig. 2(b)). Especially at the cloud base, the edges of supersaturated regions are characterized by steep gradients. The largest values of supersaturation up to $s \approx 4\%$ are found at the cloud base ($z/l_0 \approx 0.6$), while within and at the top of the cloud layer, supersaturation is mostly limited to a few tens of percent $s \lesssim 1\%$ (Figs. 2(b), 3(b)). Still, the height-dependent probability density function (PDF) of RH (Fig. 3(b)) indicates that cloud bulk and top are (super)saturated to a greater extent than the cloud base. In combination, this is results in an extremely left-side skewed, narrow peaking PDF of RH in the cloud layer (Fig. 3(b)-(d)). While the supersaturation in the cloud bulk and top seems to be rather limited, the liquid specific humidity q_l can continuously increase towards the cloud top, where it reaches its largest variability just before it falls back to $q_l = 0$ in the troposphere (Fig. 3(a)). Nonetheless, the magnitude of supersaturation in our DNSs is in general agreement with the values for cloud conditions collected in recent studies (Siebert *et al.*, 2021; Yeom *et al.*, 2021, 2024).

These observations are backed by the joint PDFs of RH and q_l, respectively vertical velocity w (Fig. 4). The largest values of supersaturation occur at relatively small q_l, while large values of q_l are associated with small supersaturation of a few tenths of percent only (Fig. 4(a)). Further, it confirms that supersaturation is predominantly associated with upward flow (Fig. 4(c)) forming a tilted, asymmetric peak around $RH = 100$. Considering the joint PDF of RH and the static energy h (Fig. 4(b)), we observe that supersaturation is characterized by values of h slightly above its cloud layer mean.

In the equilibrium case ($\mathrm{Da} = \infty$, Fig. 4(d)-(f)), it can been seen that – as set by definition – any q_l always corresponds to saturated conditions also suppressing the subsaturated part of the joint PDF (Fig. 4(d)). This essentially levels the joint PDF of RH and w around $RH = 100$ (Fig. 4(f)). In the joint PDF of RH and h, no significant difference for $RH \leq 100$ can be identified between $\mathrm{Da}_{0,n_d} = 10$ and $\mathrm{Da} = \infty$ (Fig. 4(e)). Overall, the absence of subsaturation seems to be the even larger limitation of the classical equilibrium approach compared to a finite saturation adjustment than the absence of supersaturation.

In combination, we conclude that slow saturation adjustment is a cloud accumulating effect: Supersaturation, which is related to slow condensation, occurs predominantly in the updrafts but is widely limited to a few tenths of percent except at the cloud base, where q_l is still small. However, even large portions of liquid water evaporate slowly in subsaturated regions maintaining a higher water content, which seems to surpass the effect of supersaturation. This leads to an overall accumulation of liquid water compared to instantaneous adjustment in the equilibrium approach.

CONCLUDING REMARKS & OUTLOOK

We presented an initial comparison of finite saturation adjustment ($\mathrm{Da}_{0,n_d} = 10$) versus instantaneous adjustment under phase equilibrium assumption ($\mathrm{Da} = \infty$) using 3D DNSs of a

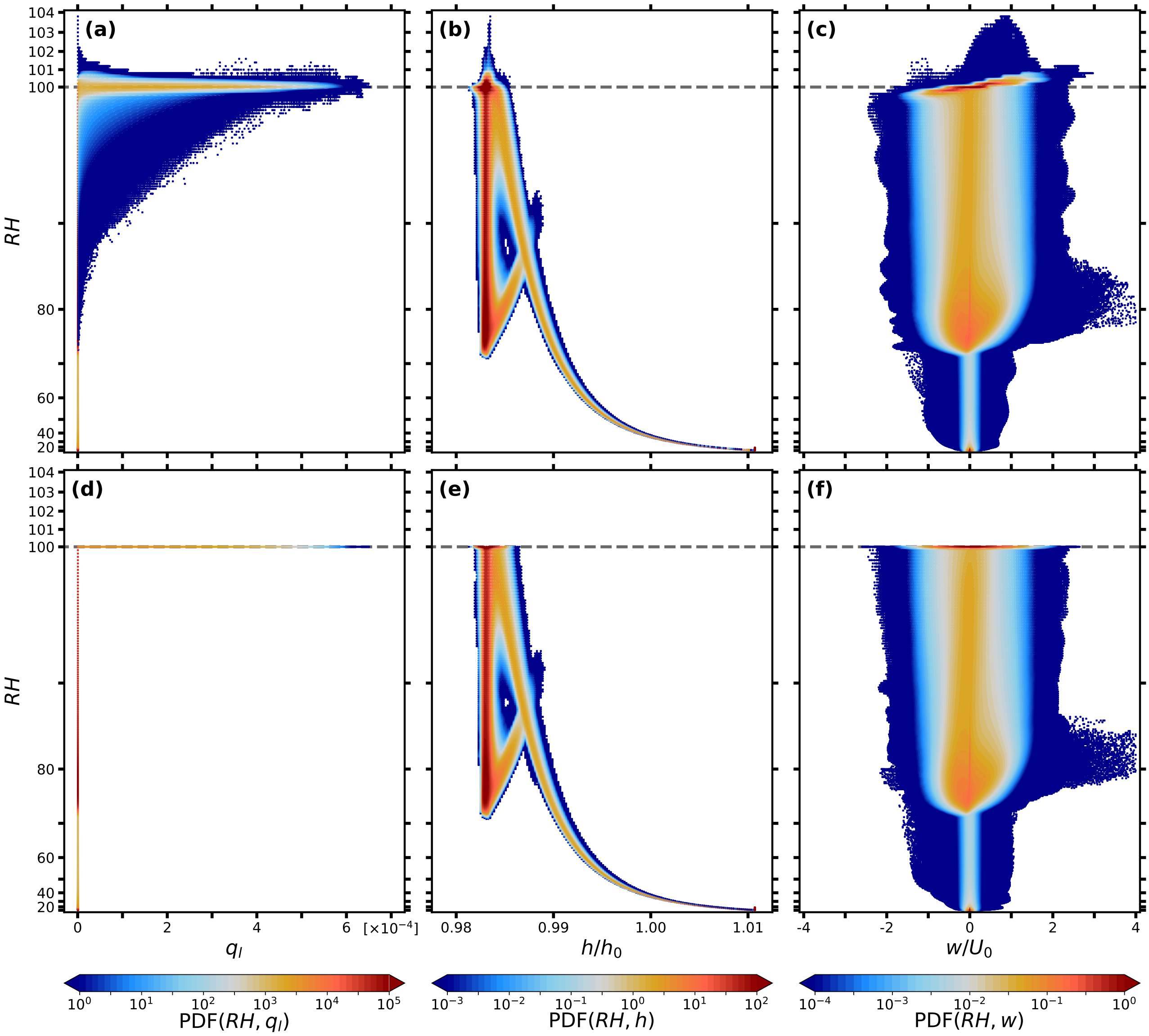

Figure 4. Joint probability density functions (PDFs) of relative humidity RH and **(a),(d)** liquid specific humidity q_l, **(b),(e)** dimensionless static energy h/h_0, and **(c),(f)** dimensionless vertical velocity w/U_0 from eight snapshots for (a)-(c) $\mathrm{Da}_{0,n_d} = 10$ and (d)-(f) $\mathrm{Da} = \infty$. The dashed line depicts $RH = 100$, above which supersaturation starts. Note the exponential axis scaling for RH to emphasize supersaturation $RH > 100$.

stratocumulus topped boundary layer with $\mathrm{Re} = 5000$ set up along the DYCOMS-II reference case, which shows how finite saturation adjustment alters the flow. Supersaturation is limited to upward transport inside the cloud layer and peaks in the updrafts at the cloud base, where q_l is still small. More crucially, analyzing the joint PDFs of RH, q_l and w, we found that subsaturation plays a bigger role than supersaturation for the cloud's water content. Based on our findings, we argue that finite saturation adjustment is cloud accumulating compared to the phase equilibrium assumption.

In the next steps, we will focus on identifying the appropriate Damköhler number that governs the dynamics of saturation adjustment. Here, we estimated the integral-scale Damköhler number as $\mathrm{Da}_{0,n_d} = 10$ based on the DYCOMS-II conditions, which for $\mathrm{Re} = 5000$ corresponds to a turbulent Damköhler number of $\mathrm{Da}_{\eta,n_d} = \mathrm{Re}^{-1/2}\mathrm{Da}_{0,n_d} \approx 0.14$. However, a realistic atmosphere is rather characterized by $\mathrm{Re} \approx 6 \cdot 10^7$, which yields $\mathrm{Da}_{\eta,n_d} \approx 1.3 \cdot 10^{-3}$. To test such Da_{η,n_d}, we will extend our parameter range of Da_{0,n_d} (Fig. 5). In addition, such an extension of the range of Da over several orders of magnitude could potentially reveal transitions between the different Da-regimes for characteristic cloud quantities like, e.g., the liquid water path, which could give us further insights on the impact of Da on the cloud's liquid water accumulation or desiccation, i.e., the evolution and lifetime of the stratocumulus clouds. As it can easily be seen, another crucial aspect in this task is the dependence on the Reynolds number Re. Therefore, we additionally aim to push Re further towards realistic atmospheric values.

In addition to the general understanding of the relevant time scales for the Damköhler number, the ultimate goal would be to obtain a simple model to represent finite saturation adjustment based on a few moments of temperature, q_t, and/or q_l, which could be used as subgrid-scale parametrization in LESs and other large-scale models. Therewith, it could be assessed how important an interacting representation of different sugrid-scale processes (like turbulence and microphysics) might be for the accuracy of such large-scale models of atmospheric flows.

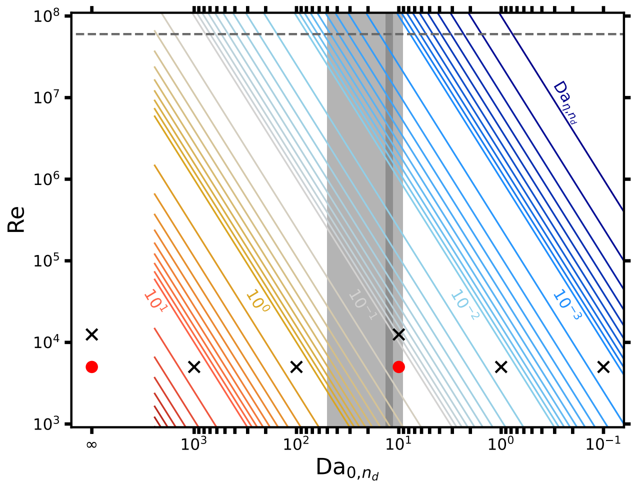

Figure 5. Parameter space of the two governing integral-scale control parameter for evaporation-condensation $\mathrm{Re} = U_0\, l_0/\nu$ and Da_{0,n_d} (see Eq. 3). The diagonal colored lines are isolines of the turbulent Damköhler number $\mathrm{Da}_{\eta,n_d} = \mathrm{Re}^{-1/2}\mathrm{Da}_{0,n_d}$. The large gray area indicates the range of Da_{0,n_d} based on typical estimates for the atmosphere ($10^3\ \mathrm{cm}^{-3} \leq n_d \leq 10^2\ \mathrm{cm}^{-3}$ and $\ln(1) \leq \sigma \leq \ln(1.5)$), while the smaller dark gray area indicates the range of Da_{0,n_d} based on the DYCOMS-II conditions ($n_d = 140\ \mathrm{cm}^{-3}$ and $\ln(1) \leq \sigma \leq \ln(1.5)$) (Ackerman *et al.*, 2004; Bretherton *et al.*, 2007; Schulz & Mellado, 2019). The dashed horizontal line at $\mathrm{Re} = 6 \cdot 10^7$ serves as a proxy for realistic atmospheric conditions. The red circles depict the 3D cases considered in the present analysis. The black crosses indicate future cases.

ACKNOWLEDGMENTS

This work received support from the Deutsche Forschungsgemeinschaft (DFG, German Research Foundation) under Germany's Excellence Strategy – EXC 2037 'CLICCS - Climate, Climatic Change, and Society' (Project Number: 390683824). We acknowledge the German Climate Computing Center (Deutsches Klimarechenzentrum, DKRZ) for granting us access to the Levante High Performance Computer (project um1276).

REFERENCES

Ackerman, A. S., Kirkpatrick, M. P., Stevens, D. E. & Toon, O. B. 2004 The impact of humidity above stratiform clouds on indirect aerosol climate forcing. *Nature* **432** (7020), 1014–1017.

Bretherton, C. S., Blossey, P. N. & Uchida, J. 2007 Cloud droplet sedimentation, entrainment efficiency, and subtropical stratocumulus albedo. *Geophys. Res. Lett.* **34** (3), 2006GL027648.

Chandrakar, K. K., Cantrell, W., Chang, K., Ciochetto, D., Niedermeier, D., Ovchinnikov, M., Shaw, R. A. & Yang, F. 2016 Aerosol indirect effect from turbulence-induced broadening of cloud-droplet size distributions. *Proc. Natl. Acad. Sci. U.S.A.* **113** (50), 14243–14248.

Cooper, W. A. 1989 Effects of Variable Droplet Growth Histories on Droplet Size Distributions. Part I: Theory. *J. Atmos. Sci.* **46** (10), 1301–1311.

Mellado, J. P. 2017 Cloud-Top Entrainment in Stratocumulus Clouds. *Annu. Rev. Fluid Mech.* **49** (1), 145–169.

Mellado, J. P., Bretherton, C. S., Stevens, B. & Wyant, M. C. 2018 DNS and LES for Simulating Stratocumulus: Better Together. *J. Adv. Model. Earth Syst.* **10** (7), 1421–1438.

Nuijens, L. & Siebesma, A. P. 2019 Boundary Layer Clouds and Convection over Subtropical Oceans in our Current and in a Warmer Climate. *Curr. Clim. Change Rep.* **5** (2), 80–94.

Pistor, R. & Mellado, J. P. 2025 Resolving Droplet Sedimentation Effects in Stratocumulus Clouds. *J. Adv. Model. Earth Syst.* **17** (8), e2025MS004966.

Rogers, R. R. & Yau, M. K. 1996 *A short course in cloud physics*, third edition edn. *International Series in Natural Philosophy* Volume 113. Burlington, Massachusetts: Butterworth-Heinemann.

Schulz, B. & Mellado, J. P. 2019 Competing Effects of Droplet Sedimentation and Wind Shear on Entrainment in Stratocumulus. *J. Adv. Model. Earth Syst.* **11** (6), 1830–1846.

Shaw, R. A. 2003 PARTICLE-TURBULENCE INTERACTIONS IN ATMOSPHERIC CLOUDS. *Annu. Rev. Fluid Mech.* **35** (1), 183–227.

Siebert, H., Szodry, K.-E., Egerer, U., Wehner, B., Henning, S., Chevalier, K., Lückerath, J., Welz, O., Weinhold, K., Lauermann, F., Gottschalk, M., Ehrlich, A., Wendisch, M., Fialho, P., Roberts, G., Allwayin, N., Schum, S., Shaw, R. A., Mazzoleni, C., Mazzoleni, L., Nowak, J. L., Malinowski, S. P., Karpinska, K., Kumala, W., Czyzewska, D., Luke, E. P., Kollias, P., Wood, R. & Mellado, J. P. 2021 Observations of Aerosol, Cloud, Turbulence, and Radiation Properties at the Top of the Marine Boundary Layer over the Eastern North Atlantic Ocean: The ACORES Campaign. *Bull. Am. Meteorol. Soc.* **102** (1), E123–E147.

Siebesma, A. P., Bony, S., Jakob, C. & Stevens, B. 2020 *Clouds and Climate: Climate Science's Greatest Challenge*, 1st edn. Cambridge University Press.

Stevens, B., Lenschow, D. H., Vali, G., Gerber, H., Bandy, A., Blomquist, B., Brenguier, J-L., Bretherton, C. S., Burnet, F., Campos, T., Chai, S., Faloona, I., Friesen, D., Haimov, S., Laursen, K., Lilly, D. K., Loehrer, S. M., Malinowski, Szymon P., Morley, B., Petters, M. D., Rogers, D. C., Russell, L., Savic-Jovcic, V., Snider, J. R., Straub, D., Szumowski, Marcin J., Takagi, H., Thornton, D. C., Tschudi, M., Twohy, C., Wetzel, M. & Van Zanten, M. C. 2003 Dynamics and Chemistry of Marine Stratocumulus—DYCOMS-II. *Bull. Amer. Meteor. Soc.* **84** (5), 579–594.

Stevens, B., Moeng, C.-H., Ackerman, A. S., Bretherton, C. S., Chlond, A., De Roode, S., Edwards, J., Golaz, J.-C., Jiang, H., Khairoutdinov, M., Kirkpatrick, M. P., Lewellen, D. C., Lock, A., Müller, F., Stevens, D. E., Whelan, E. & Zhu, P. 2005 Evaluation of Large-Eddy Simulations via Observations of Nocturnal Marine Stratocumulus. *Mon. Weather Rev.* **133** (6), 1443–1462.

Wood, R. 2012 Stratocumulus Clouds. *Mon. Weather Rev.* **140** (8), 2373–2423.

Yeom, J. M., Szodry, K.-E., Siebert, H., Ehrlich, A., Mellado, J. P., Shaw, R. A. & Yum, S. S. 2024 High-resolution measurements of microphysics and entrainment in marine stratocumulus clouds. *Q. J. R. Meteorol. Soc.* **150** (758), 81–97.

Yeom, J. M., Yum, S. S., Shaw, R. A., La, I., Wang, J., Lu, C., Liu, Y., Mei, F., Schmid, B. & Matthews, A. 2021 Vertical Variations of Cloud Microphysical Relationships in Marine Stratocumulus Clouds Observed During the ACE-ENA Campaign. *J. Geophys. Res. D: Atmos.* **126** (24), e2021JD034700.